

© 2014 by the Seismological Society of America

Kathleen McKee, David Fee, Colin Rowell, Akihiko Yokoo; Network-Based Evaluation of the Infrasonic Source Location at Sakurajima Volcano, Japan. *Seismological Research Letters* 2014;; 85 (6): 1200–1211. doi: <https://doi.org/10.1785/0220140119>

<https://doi.org/10.1785/0220140119>

Access to this work was provided by the University of Maryland, Baltimore County (UMBC) ScholarWorks@UMBC digital repository on the Maryland Shared Open Access (MD-SOAR) platform.

**Please provide feedback**

Please support the ScholarWorks@UMBC repository by emailing [scholarworks-group@umbc.edu](mailto:scholarworks-group@umbc.edu) and telling us what having access to this work means to you and why it's important to you. Thank you.

# Seismological Research Letters

## Network-based evaluation of the infrasonic source location at Sakurajima Volcano, Japan

--Manuscript Draft--

<b>Manuscript Number:</b>	SRL-D-14-00119R1
<b>Article Type:</b>	Infrasound focus section
<b>Section/Category:</b>	Regular Issue
<b>Corresponding Author:</b>	Kathleen Frances McKee, MS Alaska Volcano Observatory Fairbanks, Alaska UNITED STATES
<b>First Author:</b>	Kathleen Frances McKee, MS
<b>Order of Authors:</b>	Kathleen Frances McKee, MS
	David Fee, PhD
	Colin Rowell, MS
	Akihiko Yokoo, PhD
<b>Manuscript Region of Origin:</b>	USA

# *Seismological Research Letters*

## **COPYRIGHT/COLOR--CHARGES FORM**

**FILL OUT, SCAN, AND SUBMIT THIS FORM ONLINE WHEN SUBMITTING YOUR PAPER**

Manuscript Number: SRL-D- \_\_\_\_\_ [leave blank for new submissions]


Title: Network-based evaluation of the infrasonic source location at Sakurajima Volcano, Japan

Authors: Kathleen McKee, David Fee, Colin Rowell, Akihiko Yokoo

### **COPYRIGHT**

In accordance with Public Law 94-533, copyright to the article listed above is hereby transferred to the Seismological Society of America (for U.S. Government employees, to the extent transferable) effective if and when the article is accepted for publication in *Seismological Research Letters*. The authors reserve the right to use all or part of the article in future works of their own. In addition, the authors affirm that the article has not been copyrighted and that it is not being submitted for publication elsewhere.

To be signed by at least one of the authors (who agrees to inform the others, if any) or, in the case of "work made for hire," by the employer.

 Kathleen McKee 5-30-2014

Authorized Signature for Copyright Print Name (and title, if not author)

Date

### **COLOR CHARGES**

**Color options:** Color figures in SRL must be published in color in both the printed journal as well as in the online journal. Because the printed SRL is the journal of record, authors have no option to publish an article with figures in black and white in print but with the same figures in color online. Authors will be charged for color according to the following rate: \$1,205 for the first page, \$755 for the second page, and \$245 for each page thereafter. Articles may be submitted with some color and some black and white figures. Figures that are to be published in color must be submitted in color; figures that are to be published in black and white must be submitted in black and white. Color figures must be submitted before the paper is accepted for publication. Art guidelines are at <http://www.seismosoc.org/publications/srl/srl-contrib.php>

Check on of the options below:

Option 1. \_\_\_\_\_ I wish to publish color figures and agree to pay the color charges.

Option 2.  X  I wish to publish black and white figures only.

Send Invoice to: Business Office - Geophysical Institute - UAF  
903 Koyukuk Drive - P.O. Box 757320  
Fairbanks, Alaska 99775-7320

If your paper is accepted for publication, SSA will require you to fill out and submit an online billing/offprint-order form.

Questions regarding billing should be directed to the SSA Business Office,  
 Suite 201, Plaza Professional Building, El Cerrito, CA 94530 USA Phone 510 525-5474 Fax 510 525-7204

Rev. January 2011

# Network-based evaluation of the infrasonic source location at Sakurajima Volcano, Japan

Kathleen McKee<sup>1</sup>, David Fee<sup>1</sup>, Colin Rowell<sup>1</sup>, Akihiko Yokoo<sup>2</sup>

<sup>1</sup>*Geophysical Institute, Alaska Volcano Observatory, University of Alaska Fairbanks, Fairbanks, Alaska*

<sup>2</sup>*Aso Volcanological Laboratory, Institute for Geothermal Sciences, Graduate School of Science, Kyoto University*

## 1. Introduction

A variety of techniques have been employed to locate seismic and acoustic signals at volcanoes. A common source location method in volcano acoustics at local distance (e.g. <10 km) is semblance, a forward grid-search technique modified for volcano seismic signals by Kawakatsu et al. (2000) and Almendros and Chouet (2003). Other techniques for source location include Bayesian infrasonic source location (BISL) (Modrak et al., 2010) and time reversal acoustics (Kim and Lees, 2014). The semblance coefficient, of which this method is based, was first introduced by Neidell and Taner (1971) and defined as a time domain measure of the coherency (i.e. the similarity) of multichannel data. This method is attractive for volcano acoustic source localization, as it does not rely on a detailed velocity model, which is generally not available around volcanoes. The computation is also straightforward and resulting “semblance maps”

provide an intuitive visualization of the source location. Semblance has been applied in 2- and 3-D at a number of volcanoes, including Stromboli (Ripepe et al., 2009; Ripepe and Marchetti, 2002), Etna (Cannata et al., 2011; Montalto et al., 2010), Erebus (Jones et al., 2008), Santiaguito (Johnson et al., 2011; Jones and Johnson, 2011), and Karymsky (Rowell et al., 2014). Rowell et al. (2014) also used a time-difference-of-arrival (TDOA) localization method at Karymsky Volcano, with mixed results. At greater distances (e.g. >10 km), localization from back-azimuth cross-bearings from multiple arrays has been an effective technique (Matoza et al., 2011) but typically requires accounting for wind and atmospheric structure. In addition to source localization, semblance has also been shown effective at identifying a variety of eruption phenomena (i.e. explosive eruptions, degassing events and rockfalls) (Johnson et al., 2011). Note that all of the aforementioned methods are often limited by a relatively small number of stations and poor vertical resolution.

Here we apply the semblance technique to locate the acoustic source at the very active Sakurajima Volcano, Japan. Although extensive seismic and acoustic research has been performed at Sakurajima (Iguchi et al., 2008), source localization has not been examined in detail. Sakurajima is well known for repeated Vulcanian explosions that produce high-amplitude infrasound signals, providing an excellent volcano acoustic dataset. Sakurajima also provides an interesting opportunity as the active crater is not at the summit of the volcano and vent-station propagation paths are obstructed by topography. For comparison, Kim and Lees (2014) utilize the same dataset as we do, and apply a time reversal source imaging technique to back-propagate the acoustic wavefield and locate the acoustic source at Sakurajima Volcano.

## 2. Sakurajima Volcano

Sakurajima Volcano is the once island now peninsula due east of Kagoshima City on the island Kyushu, Japan (Fig. 1a-b). This andesitic stratovolcano has repeating Vulcanian eruptions and makes up part of the southern rim of Aira Caldera (Iguchi et al., 2008). In June 2006, Showa crater (denoted by the black triangle in Fig. 1b.), located down slope and to the east of the summit crater, reactivated after a 58-year hiatus (Yokoo et al., 2013). The transition of activity from the summit to Showa crater was gradual; initial activity ejected ash 100s of meters into the air. As activity increased starting in 2008, explosions produced ash plumes 1-4 km above the crater with bombs and occasional pyroclastic density currents extending no more than 1.5 km from the crater rim. The activity at Showa crater has been more frequent and smaller scale to that of the summit crater. Since activity recommenced, Showa crater has expanded in size; it was reported to be 289 m  $\times$  375 m in diameter in October 2013 (Japanese Ministry of Land, Infrastructure, Transport and Tourism, unpublished data).

In recent work, Yokoo et al. (2013) used a variety of instruments to improve understanding of the process leading to eruption at Showa Crater: tiltmeters and extensometers (ground deformation in strain), visual and infrared thermal cameras (temperature variations), high-sensitivity TV cameras (visual observations), broadband and short-period seismometers with some of the latter situated in boreholes (earthquakes), low-frequency microphones (infrasound waves), and miniature UV spectrometers (SO<sub>2</sub> emissions). They observed three distinct and repetitive stages leading to and followed by explosions, which we summarize here. Stage 1 starts a few hours prior to eruption (PTE) with the observance of extension in the radial and contraction in the tangential components of strain and occasionally small BH-type earthquakes

(i.e. long period earthquakes with spectral peaks in the 3-8 Hz range), which is interpreted as magma migration within Sakurajima. Stage 2 is marked by several observations in the tens of to a few minutes PTE: a distinct acceleration in strain and tilt in the same regime as stage 1, accompanied by the disappearance of glowing at the crater and a decrease in SO<sub>2</sub> release. The source of these observations is thought to be the sealing of the crater by a lava plug and the subsequent formation of a gas pressure pocket. It is the plugging of the system that builds a pocket of gas, increasing the pressure, thus accelerating the strain and tilt and preventing the escape of SO<sub>2</sub>. Stage 3 commences when the tremor amplitude increases followed by strain and tilt inversion from radial extension to contraction and tangential contraction to extension and a temperature increase observed with infrared video at a few minutes PTE. Yokoo et al. (2013) suggest the increased tremor amplitude is the result of the plug fracturing by gas pressure exceeding the rock's strength. The fractures allow gas to escape, which causes decompression that propagates down the conduit resulting in the degassing, expansion and rising of the magma. After the three stages, the eruption follows; an explosion earthquake and a preceding and main phase infrasound signal accompany it. The preceding and main phases of the infrasound are thought to be due to two components of the eruption. First, as the magma expands and rises up the conduit the resulting pressure and movement pushes the plug upwards perturbing the atmosphere, resulting in the preceding infrasonic phase. Then the gas pocket bursts through the plug launching rock fragments and creates the main phase of the infrasound wave. This two-phase infrasound signal is detailed in Yokoo et al. (2009) and Yokoo et al. (2013) and also highlighted in Fee et al. (2014). It is this main phase waveform that is used in the source location method describe herein. Shortly following this, fragmentation occurs and an ash-rich volcanic cloud is erupted. This type of activity occurs regularly at Sakurajima.

During the field campaign, discussed in the next section, Sakurajima's activity was similar to that described above and by Yokoo et al. (2013). Vulcanian-style explosions of varying size and duration were accompanied by ash-laden plumes, ash fall, meter-sized blocks and occasional volcanic lightning. Sometimes the explosions were audible with a thunder-like sound, most notably at station ARI and KUR. For the ~34 explosions recorded, the coincident ash-rich plumes ranged from 1.8 – 6.1 km above sea level (Fee et al., 2014). In many cases these explosions were followed by periods of tremor or jetting on the order of minutes to hours. A notable observation was the lack of infrasound for minutes to hours before the larger explosive events, which was also observed and in turn attributed to vent sealing by Yokoo et al. (2013).

### **3. Field Campaign**

On 18 July 2013, we deployed 5 sensors in a network configuration around Sakurajima as shown in Figure 1b. At ARI, KOM and SVO, National Center for Physical Acoustics (NCPA) digital infrasound sensors (DIS) were used, while HAR and KUR had Hyperion IFS-5201 DIS. Both sensor types have self-contained digitizers and GPS timing clocks and have flat frequency responses between ~0.02 – 250 Hz. The NCPA sensors have a pressure range of +/-1190 Pa while the Hyperion sensors are slightly narrower at +/-1000 Pa. Over the nine-day deployment, the NCPA instruments recorded at 250 Hz, while the Hyperion sensors recorded at 500 Hz. All the data were later down sampled to 200 Hz for uniformity. As is seen in Figure 1b, the network was deployed below the active vent; the maximum vertical relief across the network was 356.5 meters, between sensors HAR and SVO. In addition to the network configuration itself, the topographic profiles in Figure 1c show that in two cases the volcanic edifice is between the



active vent and the sensor. The location of Showa crater and nearby topography make Sakurajima an ideal location for evaluating the effectiveness of the semblance method in determining the infrasonic source location in the presence of topography.

#### **4. Semblance Source Location**

Here we use semblance to locate the source of infrasound signals at Sakurajima Volcano, Japan. The semblance method is a forward grid search in which the waveforms from a pair of sensors are either evaluated for coherency at each grid node as in Montalto et al. (2010); Ripepe and Marchetti (2002), or the error function is determined for each grid node as in Johnson et al. (2003); Jones et al. (2008). The node that maximizes coherency or minimizes the error function is assumed as the source. The waveforms are time-aligned assuming the signal propagates along a straight, unobstructed path between the respective grid node and sensor. Due to the straightforward application of the method it has been applied in various volcano seismic and acoustic studies. For example, Dawson et al. (2004) used radial semblance to define the shallow magmatic conduit at Kilauea volcano by locating very long period seismic events in near real-time. With infrasound data, Jones and Johnson (2011) were able to locate sub-events (different pulses) within an explosion sequence at Santiaguito Volcano, Guatemala with the semblance method. Here we apply the semblance method to individual explosive events at Sakurajima, as determined by Fee et al. (2014), as well as to consecutive time windows on the entire dataset.

The semblance calculation we use follows Rowell et al. (2014) in which the methods of Almendros and Chouet (2003), Ripepe et al. (2007) and Jones and Johnson (2011) are combined. Almendros and Chouet (2003) calculate a single 3-D semblance map by averaging the cross-

correlation coefficients for all station pairs. Ripepe et al. (2007) and Jones and Johnson (2011) then incorporated a modification. Instead of calculating semblance for all the channels at once, semblance is evaluated for each unique station pair producing semblance maps that are then multiplied together for a single map. The benefit of calculating semblance with this modification is that it suppresses side lobes and enhances the maximum semblance,  $S_m$ , location. The Rowell et al. (2014) technique takes these previous methods one step further in using a full 3-D source space rather than holding one spatial coordinate constant and calculating semblance over flat grids. The resulting single map is made up of ‘stacked’ or ‘exponential semblance’ values,  $S_e$ . For each station pair, the semblance values range from 0.5 for uncorrelated white noise to 1 for perfect coherence. When the station pair maps are stacked for the 10 unique station pairs we have at Sakurajima, the  $S_e$  values range from  $0.5^{10}=9.77 \times 10^{-4}$  to  $1^{10}=1$ . The infrasonic source location is assumed to be at the location of the peak semblance. Due to the exponential nature of the semblance values we often refer to ‘adjusted semblance’, that is

(4.1)

$$S_a = e^{\frac{\ln(S_m)}{N}},$$

in order to have a more intuitive number, where  $N$  is the number of unique station pairs. Adjusted semblance ranges from 0.5 to 1, the same as the values for a single station pair semblance map.

A variety of influencing parameters need to be accounted for when evaluating infrasonic source location using semblance, including air temperature, wind, infrasound frequency, grid spacing, and window length. To start, a grid position and volume are established. We begin with a 2.0 km

cubic grid (i.e. 8 km<sup>3</sup>) centered about Showa crater of Sakurajima volcano (Fig. 1a). The center point was determined by picking the hottest pixel from the thermal infrared Landsat 8 image (taken in August 2013) and then matching the latitude and longitude with a DEM to find the elevation. We initially chose a 50 m grid-node spacing and later decreased it to 10 m for improved resolution, but for explosive events with peak frequencies between 0.5 and 5 Hz (wavelengths ~680 m – 68 m, respectively) the former is sufficient as it is less than the peak acoustic wavelength (Rowell et al., 2014). Part of the versatility in the semblance method is that it can be ‘tuned’ to different frequencies of interest and in turn the grid-node spacing can be adjusted such that it is less than the peak acoustic wavelength (Rowell et al., 2014). In other words, higher (lower) frequencies require finer (coarser) grid-node spacing for accurate locations. With an established grid the straight-line travel times,  $dt$ , from each node to each sensor are calculated with respect to current air temperature as the sound speed,  $c$ , varies with temperature as follows:

(4.2)

$$c = 331.3 + (0.606 * T)$$

where  $T$  is temperature in degrees Celsius. Over the 9 days of data collected at Sakurajima the air temperature was recorded at a Japan Meteorological Agency (JMA) station near Kagoshima (11.6 km WSW of the crater) every 10 minutes and ranged from 25 to 35.6°C with a mean of 29.7°C. This temperature variation translates to a sound speed variation of 346 to 353 m/s with a mean of 349 m/s. For individual event source location the most recent temperature within 10 minutes was used to calculate sound speed, but for time series semblance calculations we used the average air temperature. We evaluate the effect of different sound speeds on the infrasonic

source location in Section 5. Wind can also alter sound propagation, and can thus influence the acoustic travel time. Here we incorporate wind into  $dt$  by using the effective sound speed:

(4.3)

$$c_{eff} = c + w$$

(4.4)

$$w = \mathbf{v}_w \cdot \mathbf{u}$$

where  $\mathbf{v}_w$  is the wind velocity and  $\mathbf{u}$  is the unit vector for a given grid-node to sensor combination. We then compute the effective sound speed for each grid-node and sensor path using a two-dimensional wind velocity vector. The wind speed in Kagoshima ranged from 0.3 to 8.1 m/s and varied diurnally with higher speeds at midday to early afternoon. Wind direction ranged from westerly to northerly, where westerly indicates wind coming from the west and blowing towards the east. The effect of wind on the infrasonic source location is evaluated for the selected explosive events, and we use the wind speed and direction closest to the explosion time.

Prior to applying the semblance technique, we filter the infrasound data between 0.5-5 Hz. This band encompasses the majority of the acoustic energy from Sakurajima without including the energy from the microbarom (Fig. 2b). For explosive events we divide the data into a 30 s window starting 3 s before the event times listed in Table 2 of Fee et al. (2014). This window length and start time were selected to encompass the majority of the explosion waveform across the network. For the time-series semblance we also used a 30 s sliding window as in Rowell et al. (2014), however, we used non-overlapping windows.

The sensor locations around Sakurajima are well distributed for x (easting) and y (northing) resolution (Fig. 1b), but have little vertical relief between sensors across the network ( $<10\%$  of network dimensions) (Fig. 1c). In addition, all the sensors are below the active vent, which is not uncommon for volcano sensor networks. This network configuration likely results in poor resolution in the vertical component of the source location.

## 5. Results & Discussion

Our computed semblance source locations have a general offset to the northeast of Showa crater by  $\sim 420$  m (Fig. 3). The locations vary from explosion to explosion by tens of meters, but all have a similar trend. Figure 2a shows the filtered and normalized waveforms and in Figure 3d the source location for one event (7 July 23:06:58; event 11) in the form of a 3-dimensional perspective of the three geographic planes: xy (Fig. 3a), xz (Fig. 3b), and yz (Fig. 3c), with x corresponding to east-west and y corresponding to north-south semblance slices. The maximum semblance value is included in each plane and noted by a white star; in plotting, the planes have been scaled such that the nodes with the lowest semblance values are transparent for improved viewing. The peak semblance location for this event is (70x, 60y, 250z) m, and the peak semblance value is 0.48 (corresponding to cross-correlation value of 0.93). After initial results using the coarse grid showed a general location northeast of the vent, we downsized the grid to  $x=[-0.2, 0.4]$  km,  $y=[-0.2, 0.4]$  km, and  $z=[-1, 1]$  km, where the vent is located at (0x, 0y, 0z) km, and decreased the node spacing to 10 m. The average location for all the explosive events using the finer grid and input parameters is  $\sim(80x, 73y, 9z)$  m, which is 123 m horizontally out from and  $\sim 770$  m below the vent (779 m ASL). The average offset direction has an azimuth of  $47^\circ$  and

average straight-line offset of 784 m. The first column of Table 1 lists the average semblance and location values for the 34 explosive events.

In an effort to improve the source location for the explosions and find the cause of the location offset we integrated local temperature data to improve estimates of the sound speed. We first determined the location of peak semblance using the average temperature, 29.7°C, which corresponds to a sound speed of 349.3 m/s as shown in Figure 4a (open circles) and listed in Table 1. Figure 4a is a 3-D perspective of the peak semblance locations for the 34 explosive events; three locations are plotted for each event corresponding to the different input temperatures used to calculate sound speed: 20°C, 29.7°C and current temperature within ten minutes. Incorporating local temperature data instead of using the generic 20°C improved the average vertical component of the location from 9 m ASL to 457 m ASL (770 m to 322 m below the vent) and the average straight-line distance from 784 m to 364 m. In Figure 4, the three source locations for event 28 have been connected by a line to highlight the change in source location, particularly in the vertical, by incorporating local temperature data. The adjusted peak semblance and horizontal distance changed only slightly, as shown in Table 1 and Figure 4a. The source location remained offset to the northeast, suggesting the offset is not due to variations in temperature (and hence sound speed).

Wind speed and direction data from a JMA station in Kagoshima were also incorporated into the semblance location calculation. To evaluate the necessity of including wind data, we first compared semblance locations for explosive events occurring at times of high and low wind (i.e. day and night time, respectively, due to natural diurnal wind fluctuations). Figure 5a displays

251 source locations for the 34 explosive events; daytime events are plotted as open circles, while  
252 nighttime events are solid. The nighttime locations labeled b, c, and d correspond to the  
253 waveforms from station ARI in Figure 5b, c, and d. These three events occurred at night and  
254 have the following adjusted semblance values: 0.86, 0.86 and 0.78, respectively. The seemingly  
255 similar conditions (nighttime events suggesting little to no wind, consistent explosive activity  
256 from the same vent) and high semblance values (i.e. high waveform similarity) would suggest  
257 they have similar locations, however their straight line distances vary by 10s to 100s of meters:  
258 478 m, 365 m and 305 m, respectively. These variations in the location may be due to a number  
259 of factors, such as the inherent uncertainty in the location method, network setup, and variability  
260 in the actual source location. The variation in the waveforms for these three events (Fig. 5b, c, d)  
261 suggest complex source processes at the vent that may result in differences in the actual source  
262 location. The nighttime events are evenly distributed horizontally and vertically in comparison to  
263 the daytime events. Due to the ambiguity of this comparison we incorporated 10-minute wind  
264 data into the infrasound semblance location calculation. Figure 4b shows the locations for 10-  
265 minute temperature variation (solid circles) and those that also include 10-minute wind variation  
266 (open triangles). The added wind component significantly alters the source location. The event  
267 on 19 July 02:19:11 UTC had a corresponding temperature of 32.6°C and was located at (90x,  
268 10y, 650z) m. We incorporate a wind speed of 3.6 m/s with a direction of 315° and the location  
269 changes to (10x, 80y, 70z) m. The peak semblance value remained virtually unchanged (0.932 to  
270 0.934), but the straight-line distance from the actual vent changed from 158 m to 714 m. For a  
271 different event, 20 July 23:21:50 UTC, the addition of wind (1.6 m/s, 67.5°) improves the  
272 straight-line offset distance by ~233 m, (448 m to 215 m). After incorporating wind, the average  
273 semblance value changes from 0.851 to 0.847. There are small changes in the average horizontal

location and the average straight-line offset distance drops from 364 m to 420m (Table 1 and Fig. 4b). The addition of wind into the semblance calculation influences the source location a significant amount, but it does not account for the general offset to the northeast.

In the travel time calculation for aligning the waveforms, the assumption is that the sound wave travels in a straight-line from the source to the receiver. At Sakurajima Volcano there are two source-receiver propagation paths, vent to HAR and vent to SVO, which are not line-of-sight due to the volcano summit (Fig. 1c). In these cases the sound wave must diffract around the obstruction to reach the sensors. This diffraction results in the sound energy taking a longer propagation path resulting in a greater travel time than that assumed in the semblance calculation. To evaluate the travel time offset for each station, we calculated semblance from 22-24 July in 30-second non-overlapping windows between 0.5 to 5 Hz with a grid of  $x=[0, 0.3]$  km,  $y=[0, 0.2]$  km, and  $z=[-1, 1]$  km, a grid spacing of 10 m and set an adjusted semblance threshold value of 0.7 in order to eliminate sources other than the volcano. We assumed an air temperature of 29.7°C, a corresponding sound speed of 349 m/s, and no wind. Figure 6a shows the difference between the travel time from the peak semblance location and the straight-line travel time from vent to sensor for each network station. The second column, Figure 6b, shows the distribution of travel time differences for each station. We note the average positive travel time difference for stations HAR and SVO (~0.2 seconds and ~0.22 seconds, respectively) and average negative difference for ARI, KUR and KOM (~0.09 seconds, ~0.53 seconds and ~0.32 seconds, respectively). These consistent positive and negative time differences reveal that the travel time from the source location to HAR and SVO is longer than the straight-line propagation, while it is shorter to KOM and KUR. The travel time differences are consistent and do not show diurnal



variation. This suggests the source of the differences is time invariant, with the obvious cause being topography. The lack of diurnal variation further supports temperature and wind variation as unlikely causes for the northeast location offset.

Diffraction has previously been shown to be significant in volcano acoustic scenarios (Kim and Lees, 2011; Lacanna and Ripepe, 2013). Sound waves will diffract around a barrier, such as topographic obstacles, with the amount of the diffraction related to source-receive position and the relative sizes of the acoustic wavelength and the obstacle. The longer the acoustic wavelength is, the greater proportion of sound that will refract around the obstacles (Hadden and Pierce, 1981; Pierce, 1981). Lower frequency waves should thus be less sensitive to changes in topography. To examine the frequency-dependence of diffraction at Sakurajima we filtered various explosion event waveforms in multiple frequency bands: 0.1 to 1 Hz, 1 to 5 Hz, 5 to 10 Hz and 10 to 20 Hz (corresponding to the following wavelengths 3493 m to 349.3 m, 349.3 m to 69.8 m, 69.9 m to 34.9 m, 34.9 m to 17.5 m, respectively for sound speed of 349.3 m/s at 29.7°C) (Fig. 7). The topographic obstacles between the vent and the sensors HAR and SVO are several hundred meters high and several kilometers in length (Fig. 1a, c). The scale of this topographic obstacle suggests there should be significant diffraction for the frequencies of interest at Sakurajima. Examination of the explosion signal arrival times reveals they are similar for each individual station and for all the frequency bands of interest. This suggests that these frequencies and corresponding wavelengths are all influenced by the topography (i.e. have a similar ray path).

There is other evidence of diffraction influencing the infrasound signals at Sakurajima, which we discuss here, although more in-depth discussion may be found in Fee et al. (2014), Kim and Lees (2014), and Yokoo et al. (2014). Infrasonic waveforms have been shown to be altered due to diffraction around the crater rim (Kim and Lees, 2011) and topography between the source and receiver (Lacanna and Ripepe, 2013). Figure 2a shows example waveforms from each network sensor filtered from 0.5 to 5 Hz. We observe greater high frequency content in the waveforms from ARI and KUR compared to HAR and SVO, which is also present in the PSD (Fig. 2b). This is clear for an example explosion waveform in Figure 7b, in which we observe significant differences in amplitude at higher frequencies across the network. Figure 7b shows the same frequency bands as Figure 7a, but here the amplitudes have been reduced to 1 km instead of normalized. Varying degrees of reduced rarefaction have also been observed in the Sakurajima waveforms, with stations HAR and SVO being the most significant, (Fee et al., 2014), which also suggests the influence of diffraction. Topography or a source located lower in the crater could cause this reduced rarefaction. However, we observe less high frequency content and a greater rarefaction at stations SVO and HAR, suggesting the topography of Sakurajima summit plays a more significant role in diffracting the infrasound signals.

While the semblance-derived source location is not very accurate in the presence of significant topography at Sakurajima, semblance itself may still be a useful tool. Johnson et al. (2011) used semblance to detect a variety of eruptive phenomena, even during periods of low signal-noise. Figure 8 is a pseudo-helicorder plot of 0.5 to 5 Hz data from station ARI for 23 July, overlain with 30-second non-overlapping windows of peak semblance near Showa Crater using the same parameters and threshold as in Figure 6. The scale used is adjusted semblance from 0.5 to 1,

where 0.5 corresponds to incoherent noise. Here we observe that times of eruptive activity have high semblance values while times of inactivity (or noise) have low values. This network-derived plot compares well with the pseudo-helicorder plot in Figure 3 of Fee et al. (2014), where they used small-scale infrasound array data to detect coherent infrasound signals from the active vent. The explosive events at 08:00, 20:08, 21:51, and 23:11 are well picked with high adjusted semblance values: 0.89, 0.87, 0.84 and 0.78, respectively. The longer duration tremor is also highlighted well by semblance with an average adjusted semblance value of 0.75. This suggests that semblance can be used as a tool to detect times of volcanic activity even in the presence of significant local topography.

## **6. Conclusions**

We performed network-based 3-D location of infrasound sources at Sakurajima Volcano using the semblance technique. The source locations are generally offset to the northeast of the active vent (Showa crater) between approximately 129 to 133 m in the xy plane with a straight-line offset of 364 to 420 m. Vertical resolution of the source location is poor, likely due to a generally 2-D network all located below the vent. We incorporated hourly temperature data to estimate more realistic sound speeds, which improved the source locations but did not correct the offset. Wind speed and direction are also integrated into the semblance method and reveal that although wind can significantly influence the source location at Sakurajima Volcano, it also does not account for the general location offset. These results suggest realistic temperature and wind estimates should be considered in future volcano acoustic source localizations techniques. Analysis of the travel time variance between each network station and the vent shows consistent time differences at each station and no diurnal variation. This evidence, along with analysis of

the frequency content of the waveforms from each station and the station-vent profiles, suggests diffraction around topography plays a significant role in the semblance location offset at Sakurajima

Ultimately, semblance is limited in regions of complex topography where there is not a direct acoustic propagation path between source-receiver, and other methods such as full waveform simulation and time reversal source imaging (e.g. Kim and Lees (2014)) should be used. The semblance technique can still be useful for identifying times of coherent infrasound and effective at other locations with less significant topography and direct propagation paths.

## **7. Acknowledgements**

We would like to thank the Sakurajima Volcano Research Center (SVO), Mie Ichihara, and Yuki Abe for assistance with data collection and planning, as well as Jeff Johnson, Philippa Demonte, Brian Terbush, and Robin Matoza. Funding was provided by NSF grant EAR-1113294 and the Geophysical Institute. The manuscript was significantly improved by two helpful reviews.

## **Figure Captions**

- 1) a) Map of Japan with Sakurajima Volcano highlighted by the triangle. b) 3-D view of Sakurajima Volcano with infrasound network station locations denoted by dots and vent denoted by triangle. Infrasound sources were initially searched for within the 2 km x 2 km x 2 km box. c) Sensor to vent profiles for each network station. Note the significant topographic obstructions present for stations SVO and HAR.

- 2) Normalized waveform from each network station for the explosive event on 20 July 23:06:58 UTC filtered from 0.5 to 5 Hz. Stated amplitudes are the peak pressures at each station for the event. Waveforms are in order of increasing distance from the vent. b) Power spectral density for the event in Figure 2a.
- 3) Source location and semblance maps for an explosive event on 20 July 23:06:58 UTC. The white star denotes the location of peak semblance in a) map view, b) east-west and vertical map, c) north-south and vertical map, and d) 3-D perspective of semblance source location map with the three planes that contain the peak semblance values displayed. Note the semblance values have been transparently scaled such that the lowest values are not visible.
- 4) Semblance source locations plotted for the 34 explosive events. Each event has a different shade. The large black circle with the gray outline denotes Showa crater. a) Comparison of the source locations for various temperature parameters: 20°C (stars), 29.7°C - average temperature (open circles) and 10-minute temperature data (closed circles). b) Source location comparison between 10-minute temperature data (closed circles) and incorporating 10-minute wind data (open triangles). In both a) and b) a single event's source location has been connected by a line to highlight how the location varies after incorporating local temperature and wind data.
- 5) a) Comparison of the semblance source locations for events that occurred during the day (open circles) and night (closed circles) using 10-minute temperature data. b) Waveforms from three nighttime events; the time is the start of the window with the time axis in turn being absolute time. The waveforms correspond to the black dot labeled b, c, or d in the location plot.

- 6) Travel-time difference between the expected source location and the calculated source location for each station. The first column (a) shows the change in relative travel time (travel time found by semblance minus straight-line) in seconds for each network station for a two day period, 22 July 03:00:00 to 24 July 00:00:00 UTC. The second column (b) is the distribution of the change for each station, where  $\mu$  is the mean,  $\sigma$  is the standard deviation and  $\delta$  tt stands for relative change in travel time. N is the number of 30-second windows that semblance was calculated above the threshold.
- 7) Waterfall plots of straight-line, time-shifted waveforms for the explosive event on 20 July 23:06:55 in four different frequency bands: a) amplitude normalized, b) amplitude reduced to 1 km. The time axes are absolute time.
- 8) Pseudo-helicorder plot of data from station ARI on 23 July 2013. Data are filtered from 0.5 to 5 Hz and overlain with 30-second windows of semblance results. The scale is adjusted semblance, such that 0.5 corresponds to incoherent noise and 1 is perfect coherency. The lower bound of the color bar is set below the threshold so that values at or above the threshold have color.

**Table 1 The average, minima and maxima values for semblance, horizontal distance, 3D distance, azimuth and vertical location for the 34 explosive events of the dataset with respect to different temperature parameters and wind**

	20 C	10 min Mean Temperature 29.7 C	10 minute Variation	10 minute Variation with wind
--	------	--------------------------------------	------------------------	-------------------------------------

<b>Adjusted Peak Semblance, Average</b>	0.863	0.852	0.851	0.847
<b>Adjusted Peak Semblance, Min.</b>	0.655	0.648	0.646	0.643
<b>Adjusted Peak Semblance, Max.</b>	0.934	0.934	0.932	0.934
<b>Horizontal Distance, Average [m]</b>	122.97	129.17	128.75	132.84
<b>Horizontal Distance, Min. [m]</b>	78.10	76.16	76.16	64.03
<b>Horizontal Distance, Max. [m]</b>	272.03	238.54	246.98	250.00
<b>3D Distance, Average [m]</b>	783.97	366.92	363.92	420.40
<b>3D Distance, Min. [m]</b>	358.00	209.38	157.86	215.02
<b>3D Distance, Max. [m]</b>	985.05	641.99	708.41	713.87
<b>Azimuth, Average</b>	46.68	67.18	68.27	57.47
<b>Azimuth, Min.</b>	-53.97	-56.98	-58.24	-53.13
<b>Azimuth, Max.</b>	79.70	94.40	94.40	104.04
<b>Vertical Location, Average [m ASL]</b>	8.53	447.65	456.76	413.82

<b>Vertical Location, Min. [m ASL]</b>	- 200.00	170.00	100.00	70.00
<b>Vertical Location, Max. [m ASL]</b>	470.00	880.00	1020.00	1020.00

430



## References:

- Almendros, J., and B. Chouet (2003). Performance of the Radial Semblance Method for the Location of Very Long Period Volcanic Signals, *Bulletin of the Seismological Society of America* **93** 1890-1903, 10.1785/0120020143.
- Cannata, A., P. Montalto, M. Aliotta, C. Cassisi, A. Pulvirenti, E. Privitera, and D. Patanè (2011). Clustering and classification of infrasonic events at Mount Etna using pattern recognition techniques, *Geophysical Journal International* **185** 253-264, 10.1111/j.1365-246X.2011.04951.x.
- Dawson, P., D. Whilldin, and B. Chouet (2004). Application of near real-time radial semblance to locate the shallow magmatic conduit at Kilauea Volcano, Hawaii, *Geophysical Research Letters* **31**, 10.1029/2004GL021163.
- Fee, D., A. Yokoo, and J. B. Johnson (2014). Introduction to an open community infrasound dataset from the actively erupting Sakurajima Volcano, Japan, *Seismological Research Letters*,
- Hadden, W. J., and A. D. Pierce (1981). Sound Diffraction around Screens and Wedges for Arbitrary Point-Source Locations, *Journal of the Acoustical Society of America* **69** 1266-1276, 10.1121/1.385809.
- Iguchi, M., H. Yakiwara, T. Tameguri, M. Hendrasto, and J.-i. Hirabayashi (2008). Mechanism of explosive eruption revealed by geophysical observations at the Sakurajima, Suwanosejima and Semeru volcanoes, *Journal of Volcanology and Geothermal Research* **178** 1-9, 10.1016/j.jvolgeores.2007.10.010.
- Johnson, J. B., R. C. Aster, M. C. Ruiz, S. D. Malone, P. J. McChesney, J. M. Lees, and P. R. Kyle (2003). Interpretation and utility of infrasonic records from erupting volcanoes, *Journal of Volcanology and Geothermal Research* **121** 15-63, 10.1016/S0377-0273(02)00409-2.
- Johnson, J. B., J. Lees, and N. Varley (2011). Characterizing complex eruptive activity at Santiaguito, Guatemala using infrasound semblance in networked arrays, *Journal of Volcanology and Geothermal Research* **199** 1-14, 10.1016/j.jvolgeores.2010.08.005.
- Jones, K. R., and J. B. Johnson (2011). Mapping complex vent eruptive activity at Santiaguito, Guatemala using network infrasound semblance, *Journal of Volcanology and Geothermal Research* **199** 15-24, 10.1016/j.jvolgeores.2010.08.006.
- Jones, K. R., J. B. Johnson, R. Aster, P. R. Kyle, and W. C. McIntosh (2008). Infrasonic tracking of large bubble bursts and ash venting at Erebus Volcano, Antarctica, *Journal of Volcanology and Geothermal Research* **177** 661-672, 10.1016/j.jvolgeores.2008.02.001.
- Kawakatsu, H., S. Kaneshima, H. Matsubayashi, T. Ohminato, Y. Sudo, T. Tsutsui, K. Uhira, H. Yamasato, H. Ito, and D. Legrand (2000). Aso94: Aso seismic observation with broadband instruments, *Journal of Volcanology and Geothermal Research* **101** 129-154, 10.1016/S0377-0273(00)00166-9.

467 Kim, K., and J. Lees (2014). Local Volcano Infrasound and Source Localization Investigated by  
468 3D Simulation, *Seismological Research Letters*,

469 Kim, K., and J. M. Lees (2011). Finite-difference time-domain modeling of transient infrasonic  
470 wavefields excited by volcanic explosions, *Geophysical Research Letters* **38**,  
471 10.1029/2010gl046615.

472 Lacanna, G., and M. Ripepe (2013). Influence of near-source volcano topography on the acoustic  
473 wavefield and implication for source modeling, *Journal of Volcanology and Geothermal*  
474 *Research* **250** 9-18, 10.1016/j.jvolgeores.2012.10.005.

475 Matoza, R. S., A. Le Pichon, J. Vergoz, P. Herry, J.-M. Lalande, H.-i. Lee, I.-Y. Che, and A.  
476 Rybin (2011). Infrasonic observations of the June 2009 Sarychev Peak eruption, Kuril Islands:  
477 Implications for infrasonic monitoring of remote explosive volcanism, *Journal of Volcanology*  
478 *and Geothermal Research* **200** 35-48, 10.1016/j.jvolgeores.2010.11.022.

479 Modrak, R. T., S. J. Arrowsmith, and D. N. Anderson (2010). A Bayesian framework for  
480 infrasound location, *Geophysical Journal International* **181** 399-405, 10.1111/j.1365-  
481 246X.2010.04499.x.

482 Montalto, P., A. Cannata, E. Privitera, S. Gresta, G. Nunnari, and D. Patanè (2010). Towards an  
483 Automatic Monitoring System of Infrasonic Events at Mt. Etna: Strategies for Source Location  
484 and Modeling, *Pure and Applied Geophysics* **167** 1215-1231, 10.1007/s00024-010-0051-y.

485 Neidell, N. S., and M. T. Taner (1971). Semblance and other coherency measures for  
486 multichannel data, *Geophysics* **36** 482-497, 10.1190/1.1440186.

487 Pierce, A. D. (1981). *Acoustics: An Introduction to Its Physical Principles and Applications*,  
488 McGraw-Hill New York.

489 Ripepe, M., D. Delle Donne, G. Lacanna, E. Marchetti, and G. Ulivieri (2009). The onset of the  
490 2007 Stromboli effusive eruption recorded by an integrated geophysical network, *Journal of*  
491 *Volcanology and Geothermal Research* **182** 131-136, 10.1016/j.jvolgeores.2009.02.011.

492 Ripepe, M., and E. Marchetti (2002). Array tracking of infrasonic sources at Stromboli volcano,  
493 *Geophysical Research Letters* **29** 2076, 10.1029/2002gl015452.

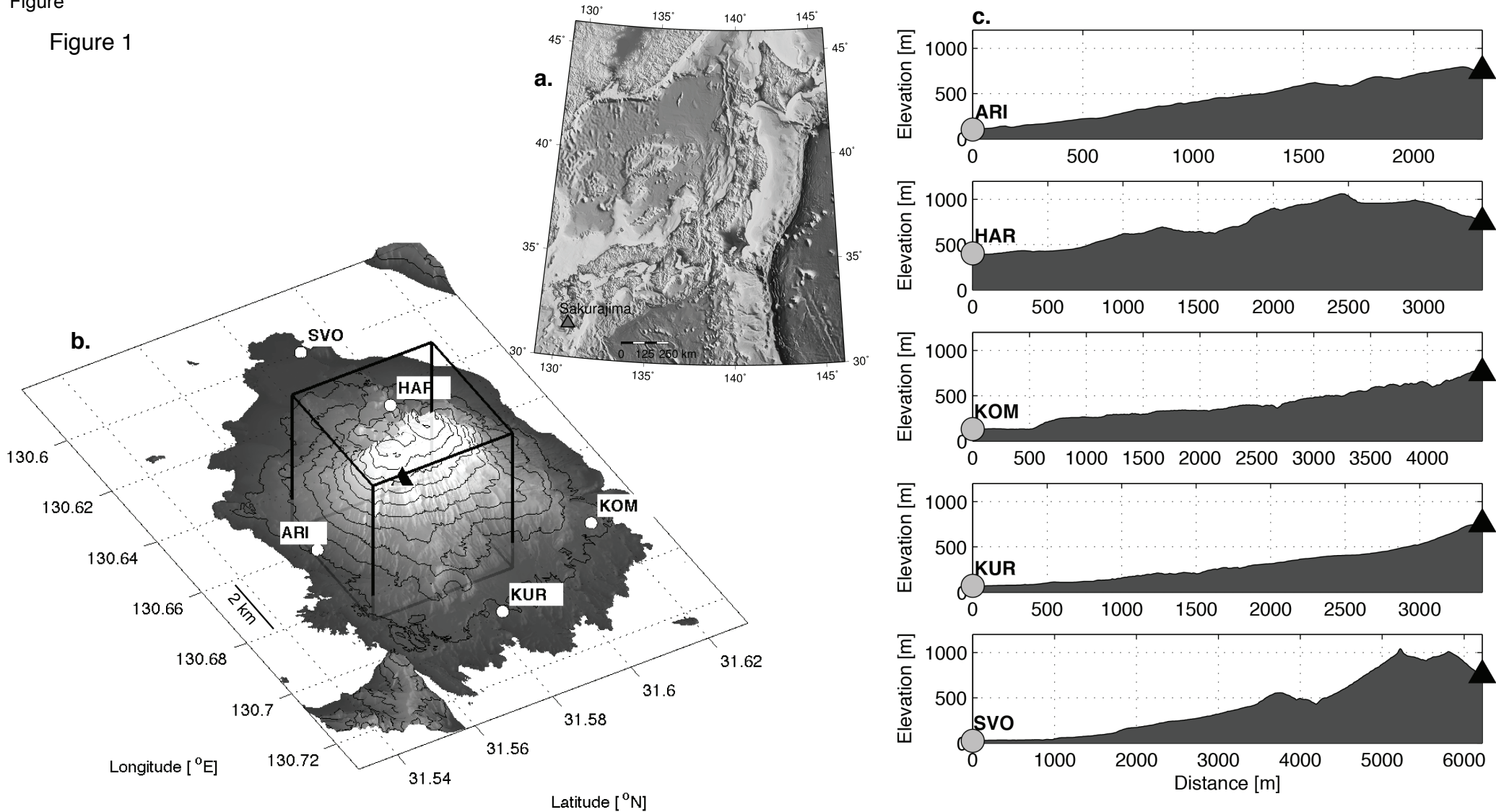
494 Ripepe, M., E. Marchetti, and G. Ulivieri (2007). Infrasonic monitoring at Stromboli volcano  
495 during the 2003 effusive eruption: Insights on the explosive and degassing process of an open  
496 conduit system, *Journal of Geophysical Research* **112**, 10.1029/2006JB004613.

497 Rowell, C., D. Fee, C. A. Szuberla, K. M. Arnoult, R. S. Matoza, P. P. Firstov, K. Kim, and E.  
498 Makhumlov (2014). Three-dimensional volcano-acoustic source localization at Karymsky  
499 Volcano, Kamchatka, Russia, *Journal of Volcanology and Geothermal Research* **283** 101-115,  
500 10.1016/j.jvolgeores.2014.06.015.

501 Yokoo, A., M. Iguchi, T. Tameguri, and K. Yamamoto (2013). Processes Prior to Outbursts of  
 502 Vulcanian Eruption at Showa Crater of Sakurajima Volcano, Bulletin of the Volcanological  
 503 Society of Japan **58** 163-181,  
  
 504 Yokoo, A., Y. J. Suzuki, and M. Iguchi (2014). Dual infrasound sources at Vulcanian eruption of  
 505 Sakurajim volcano inferred from cross-array observation, Seismological Research Letters,  
  
 506 Yokoo, A., T. Tameguri, and M. Iguchi (2009). Swelling of a lava plug associated with a  
 507 Vulcanian eruption at Sakurajima Volcano, Japan, as revealed by infrasound record: case study  
 508 of the eruption on January 2, 2007, Bulletin of volcanology **71** 619-630, 10.1007/s00445-008-  
 509 0247-5.  
 510  
 511

Figure

Figure 1



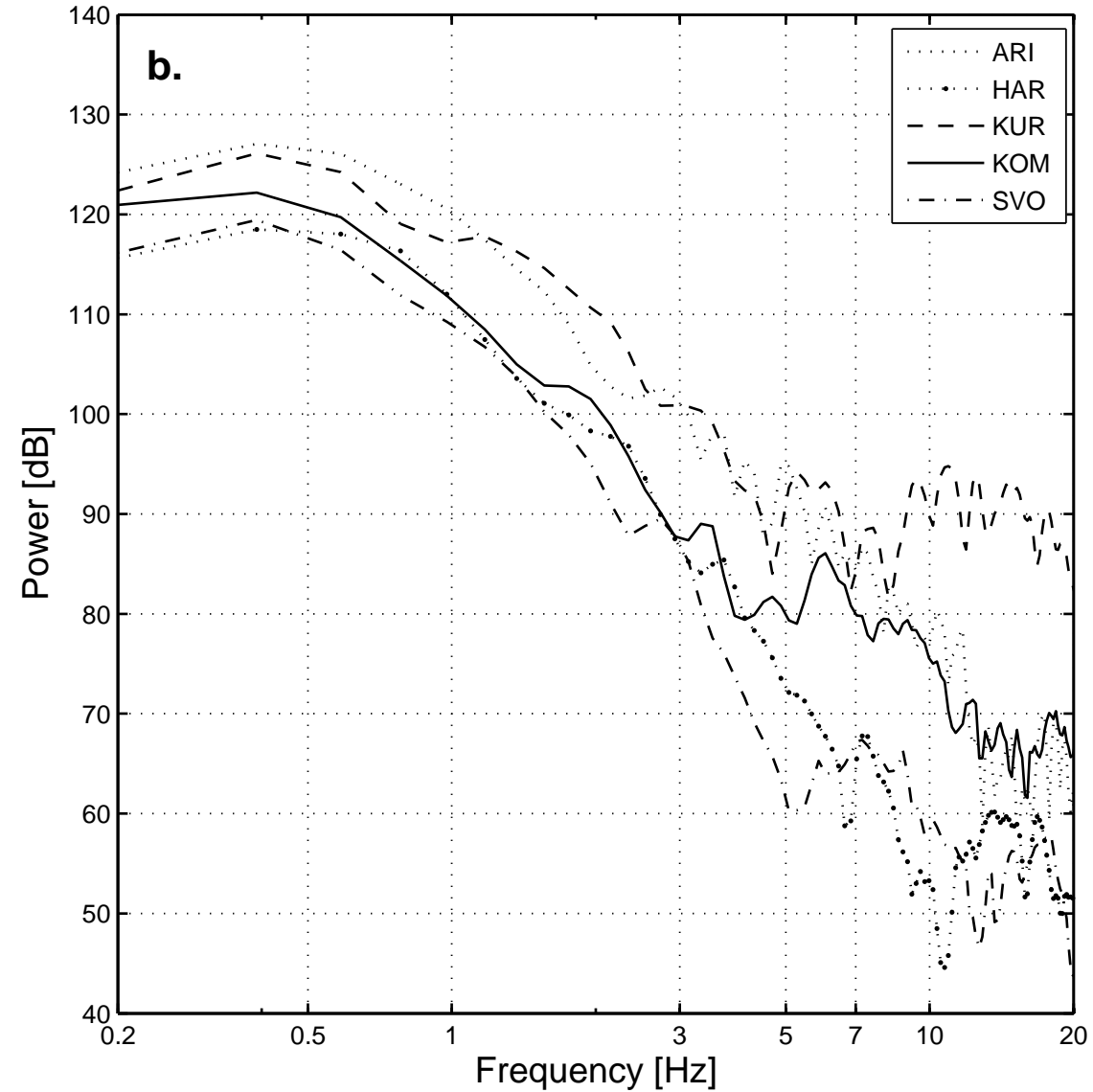
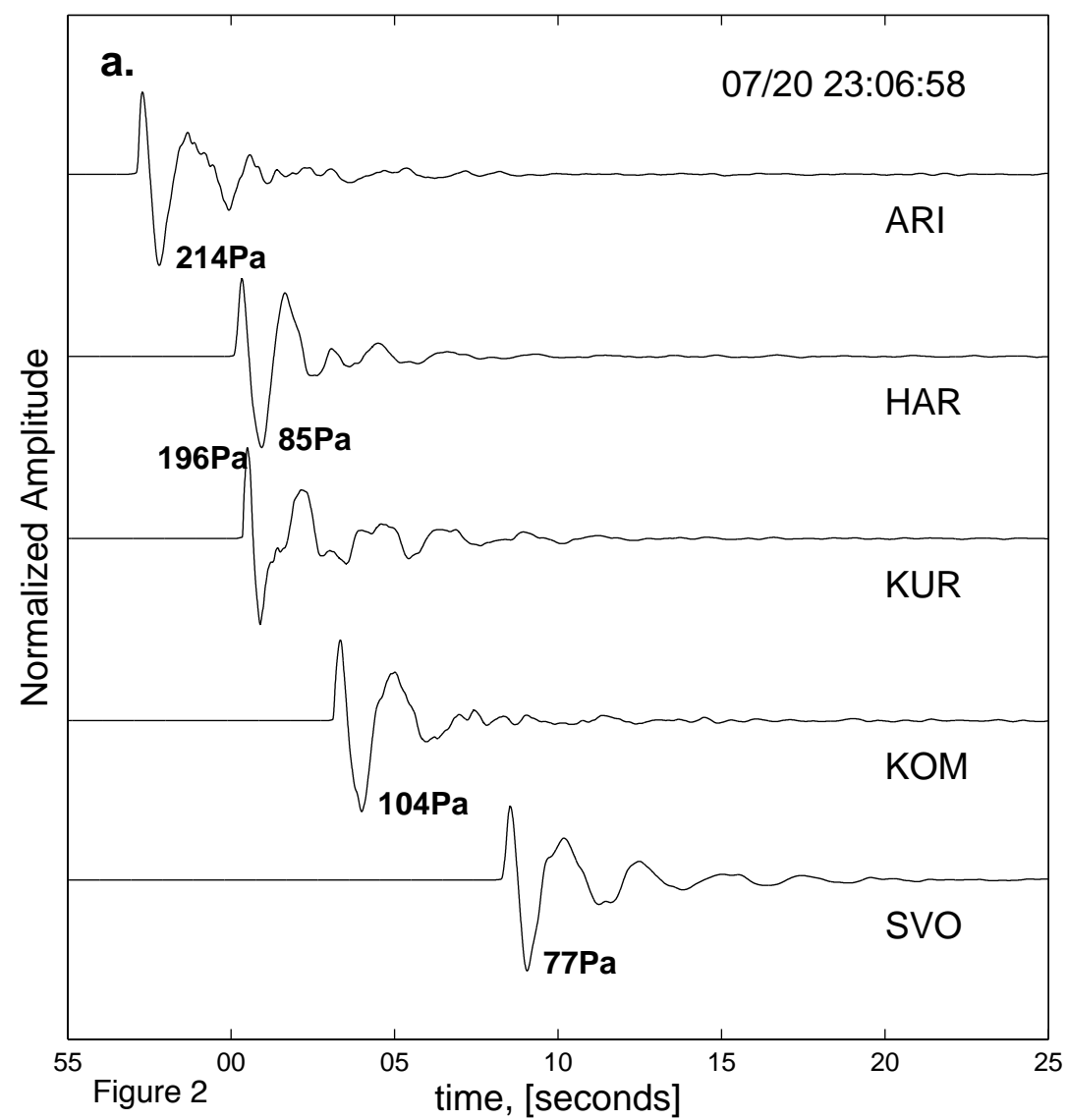
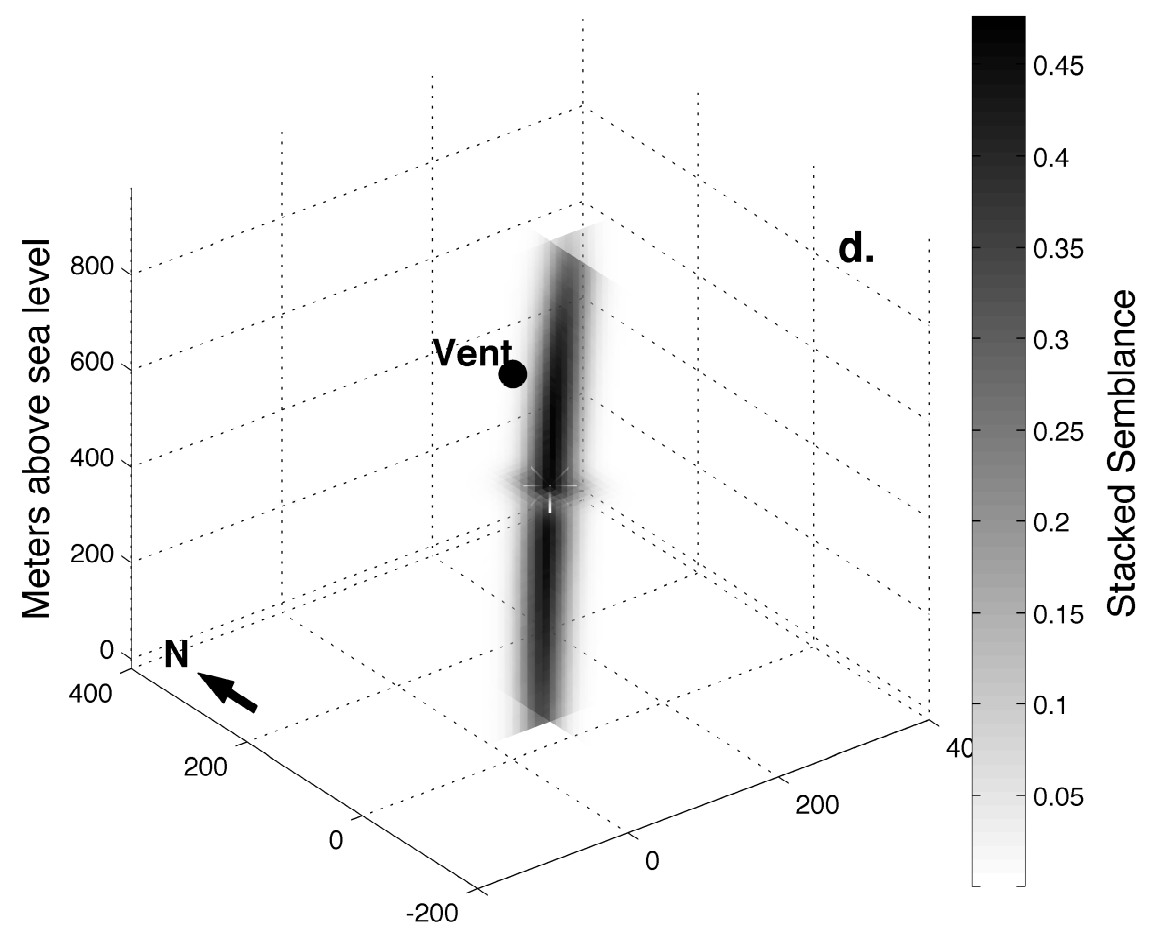
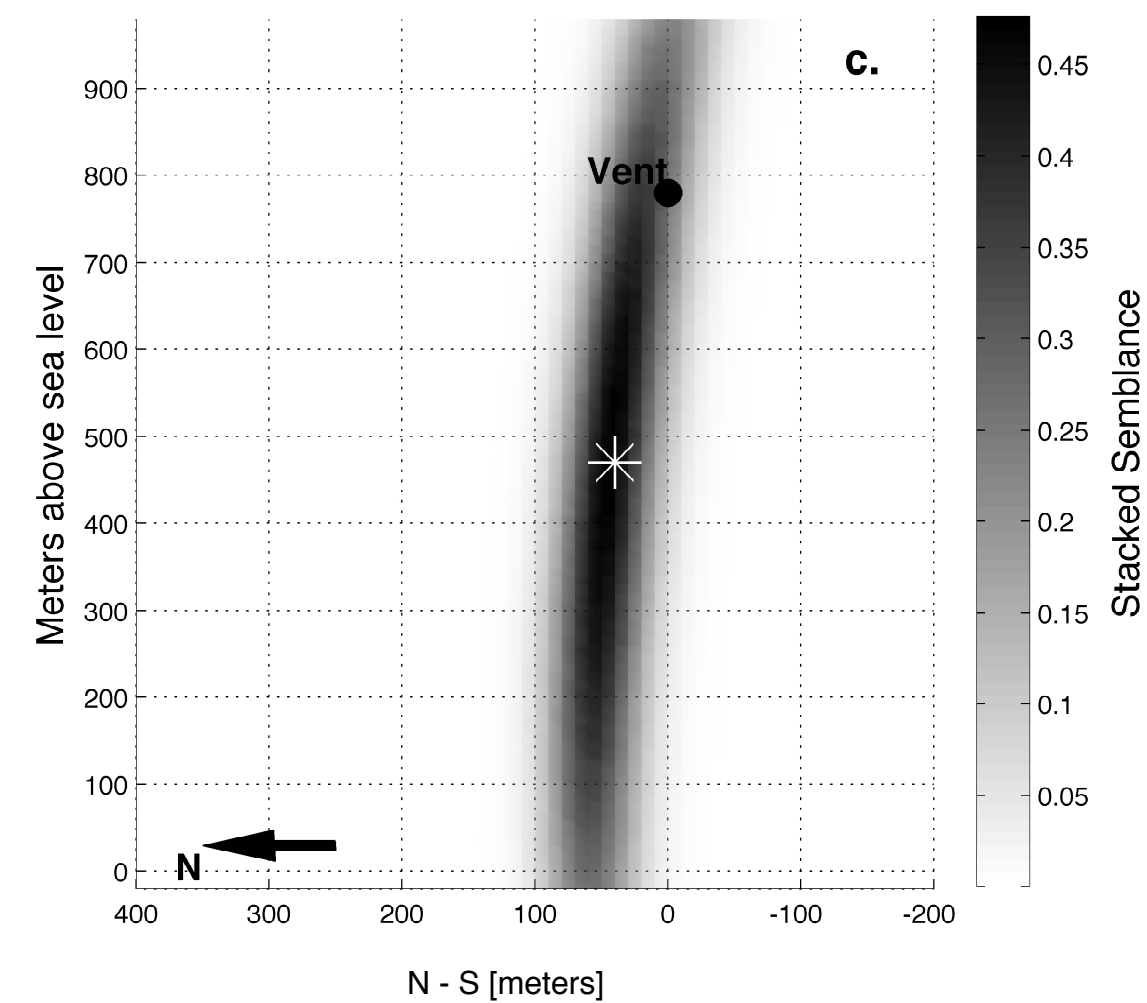
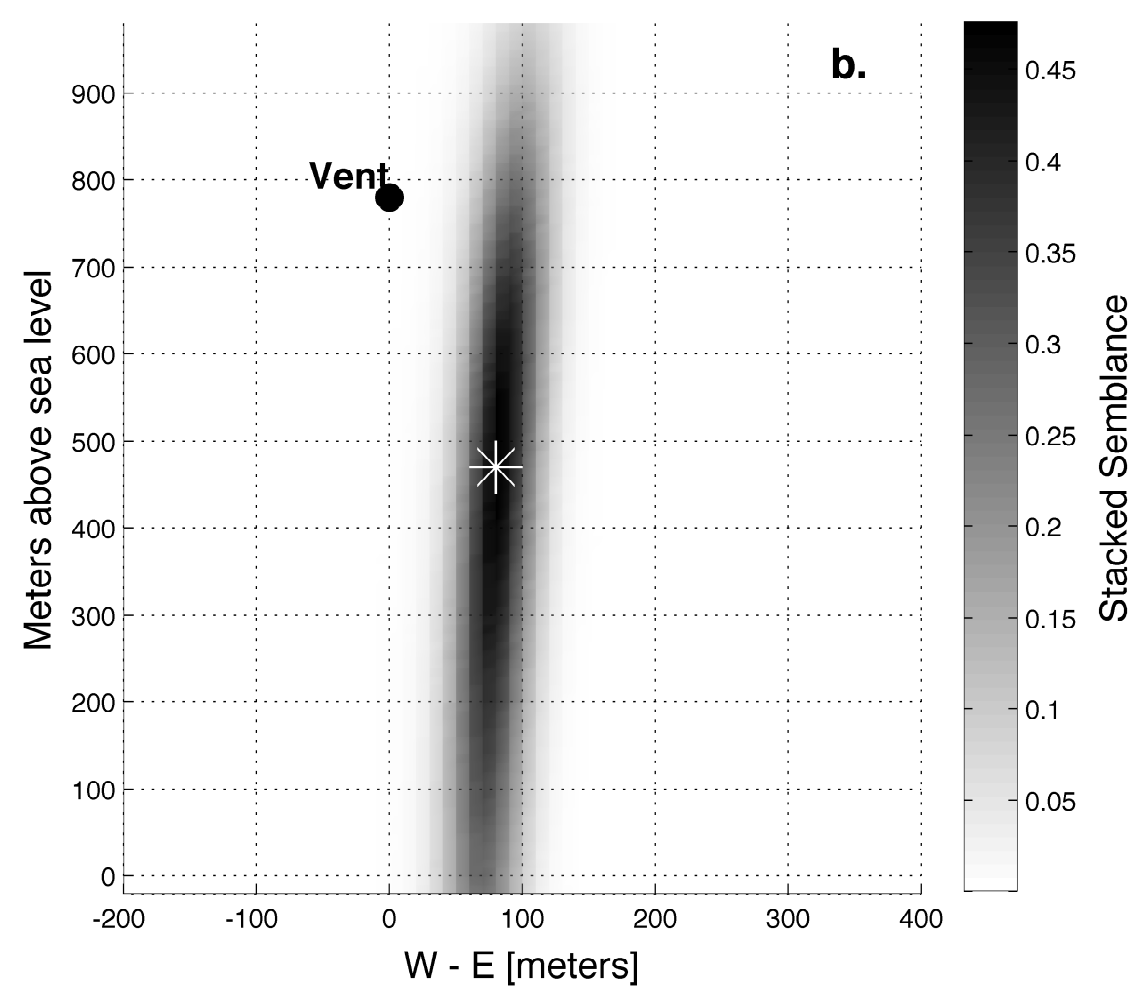
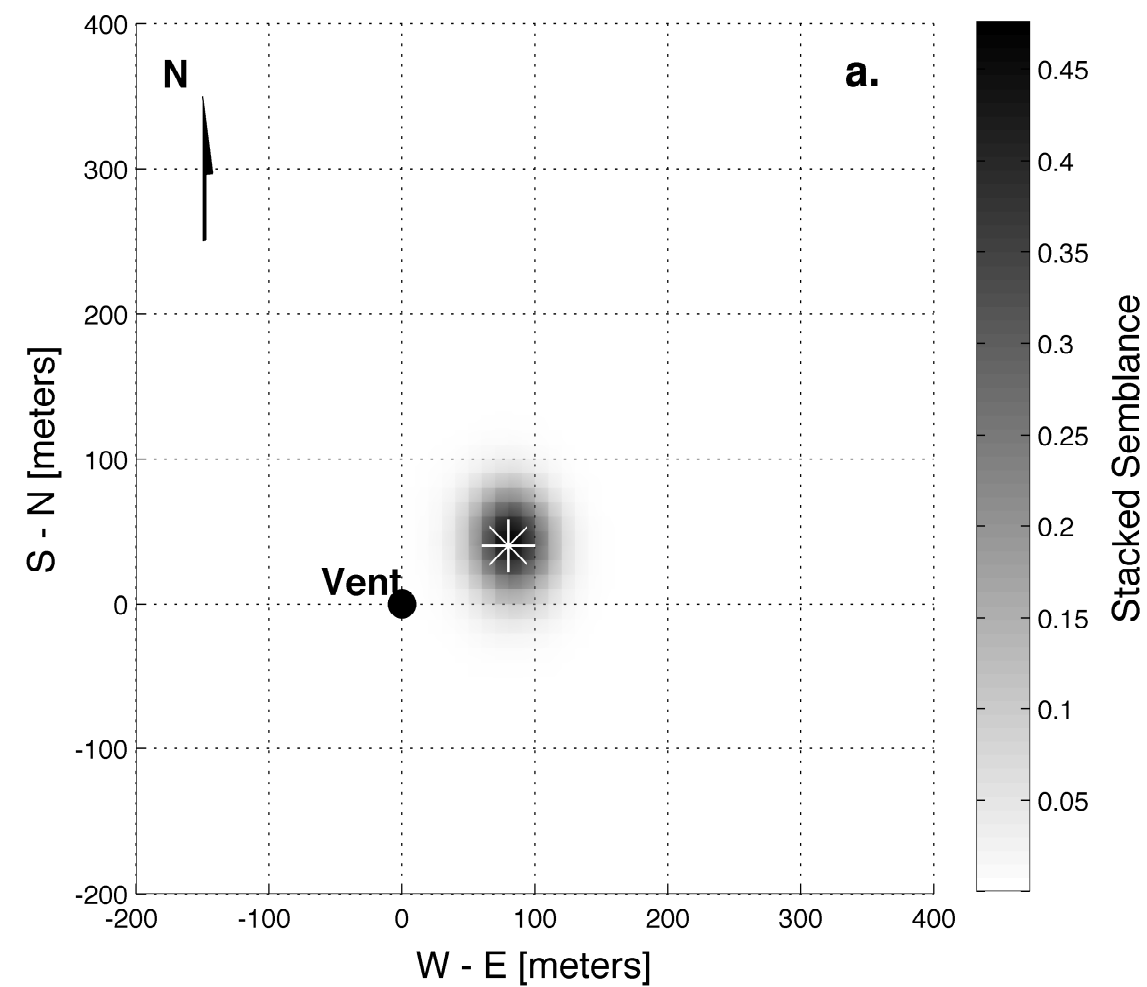


Figure 3



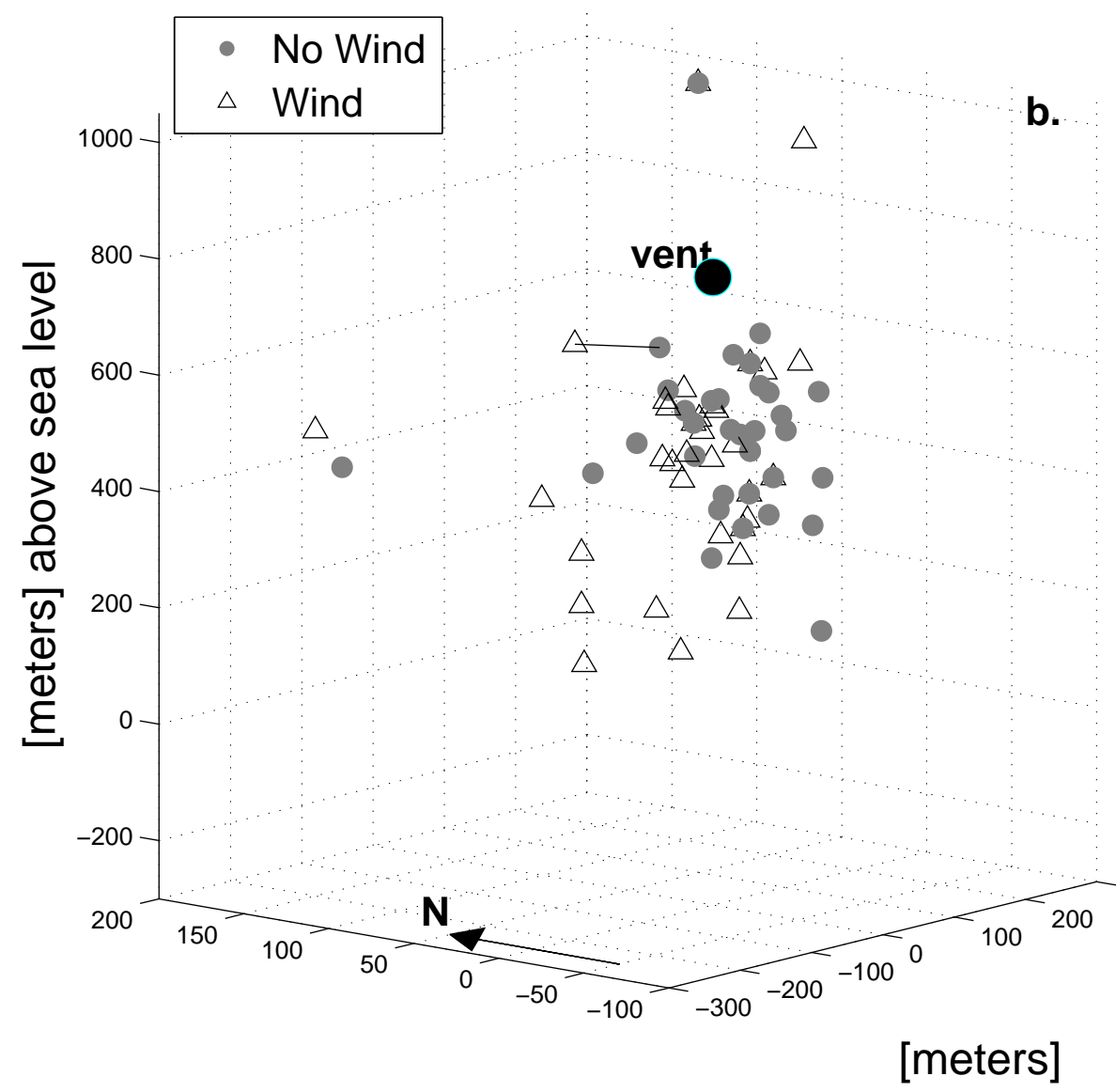
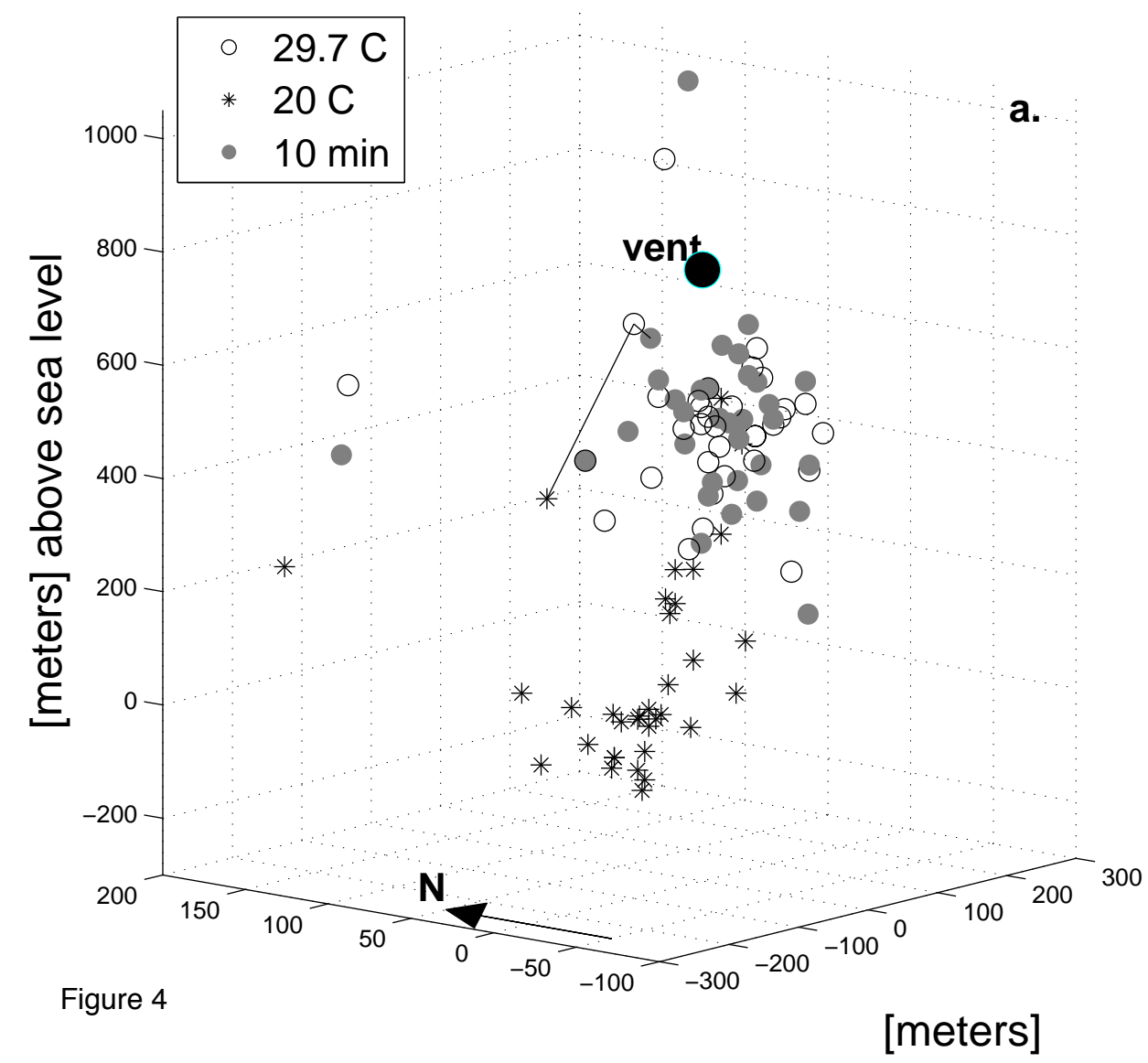
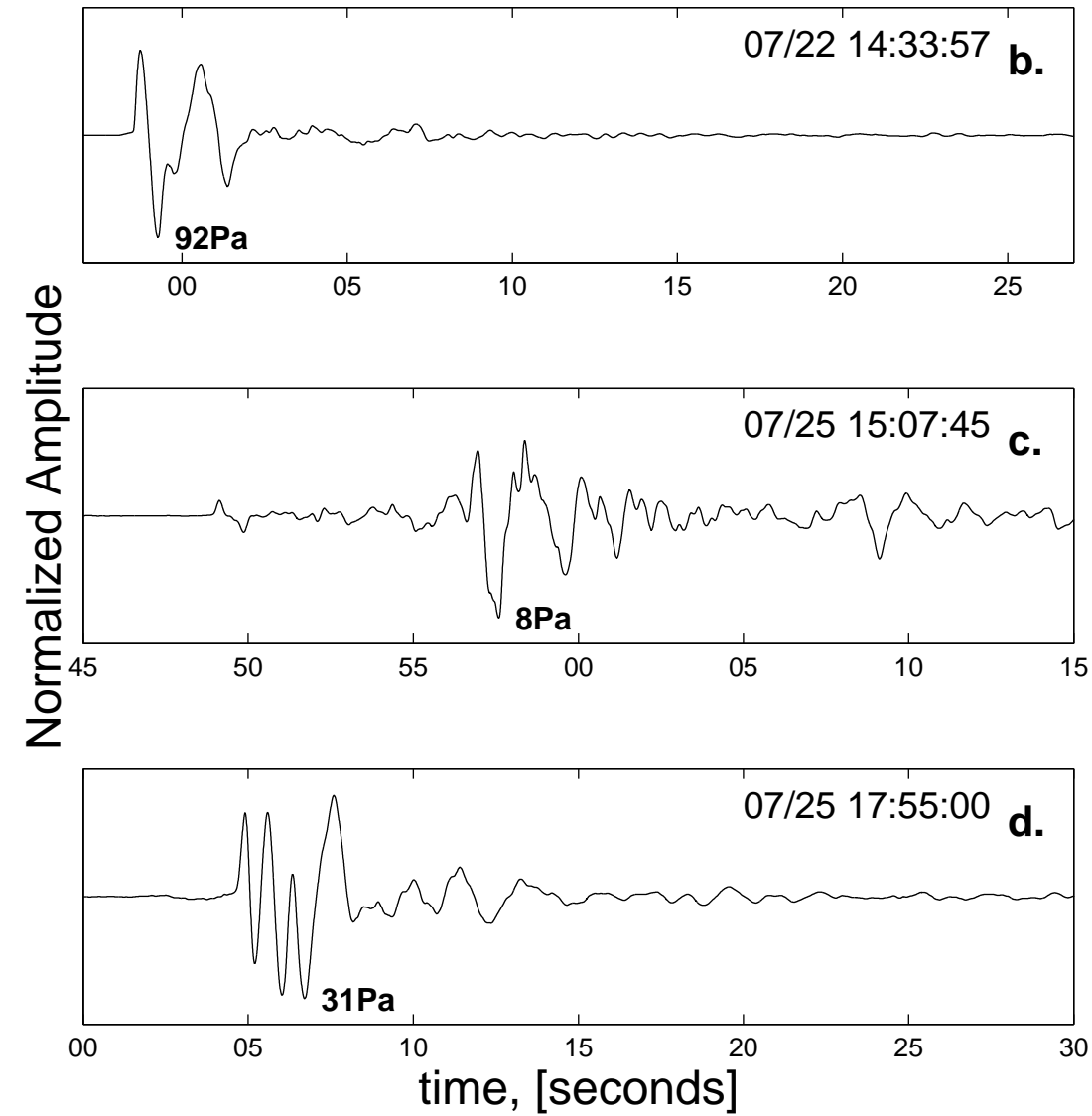
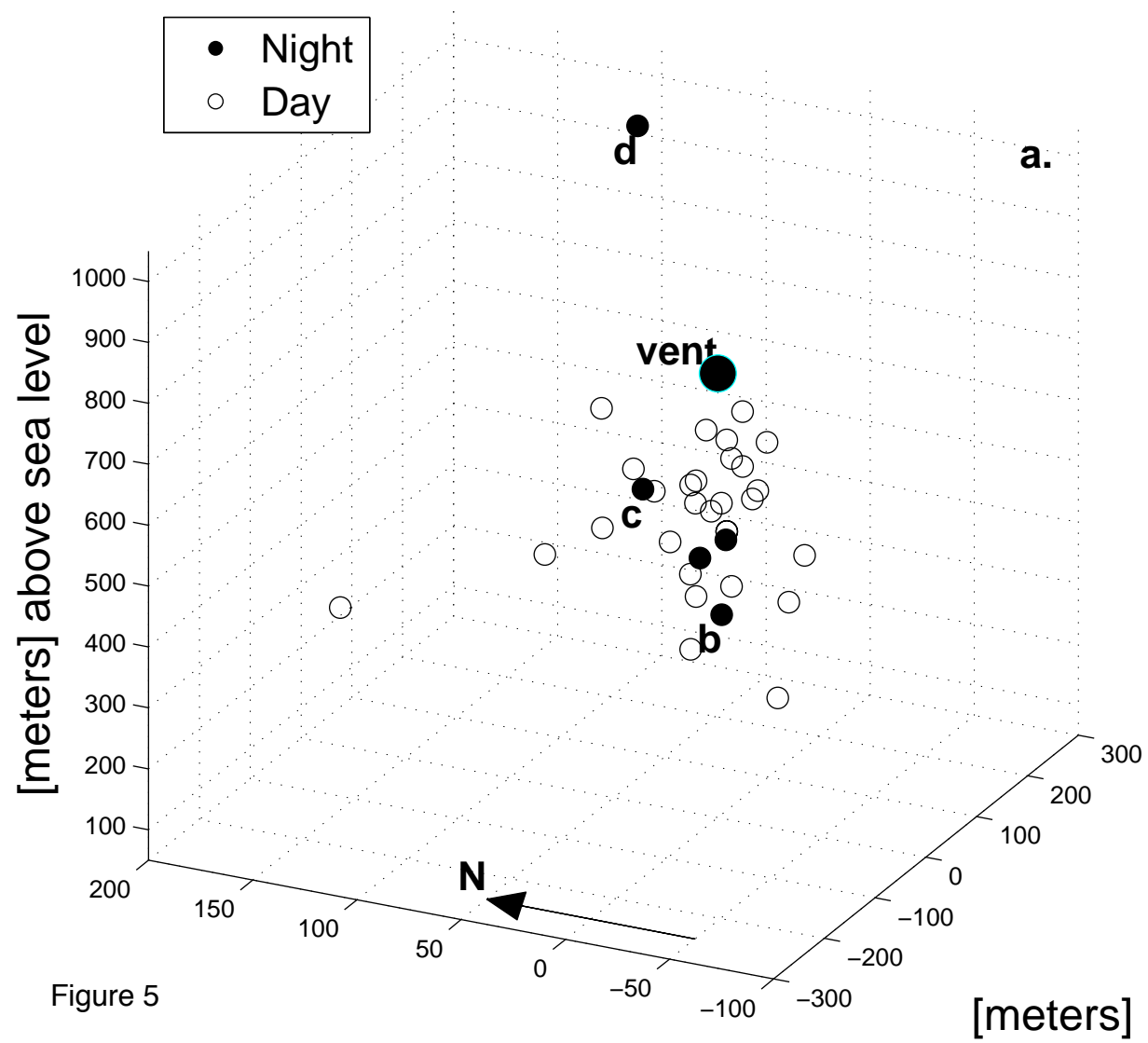
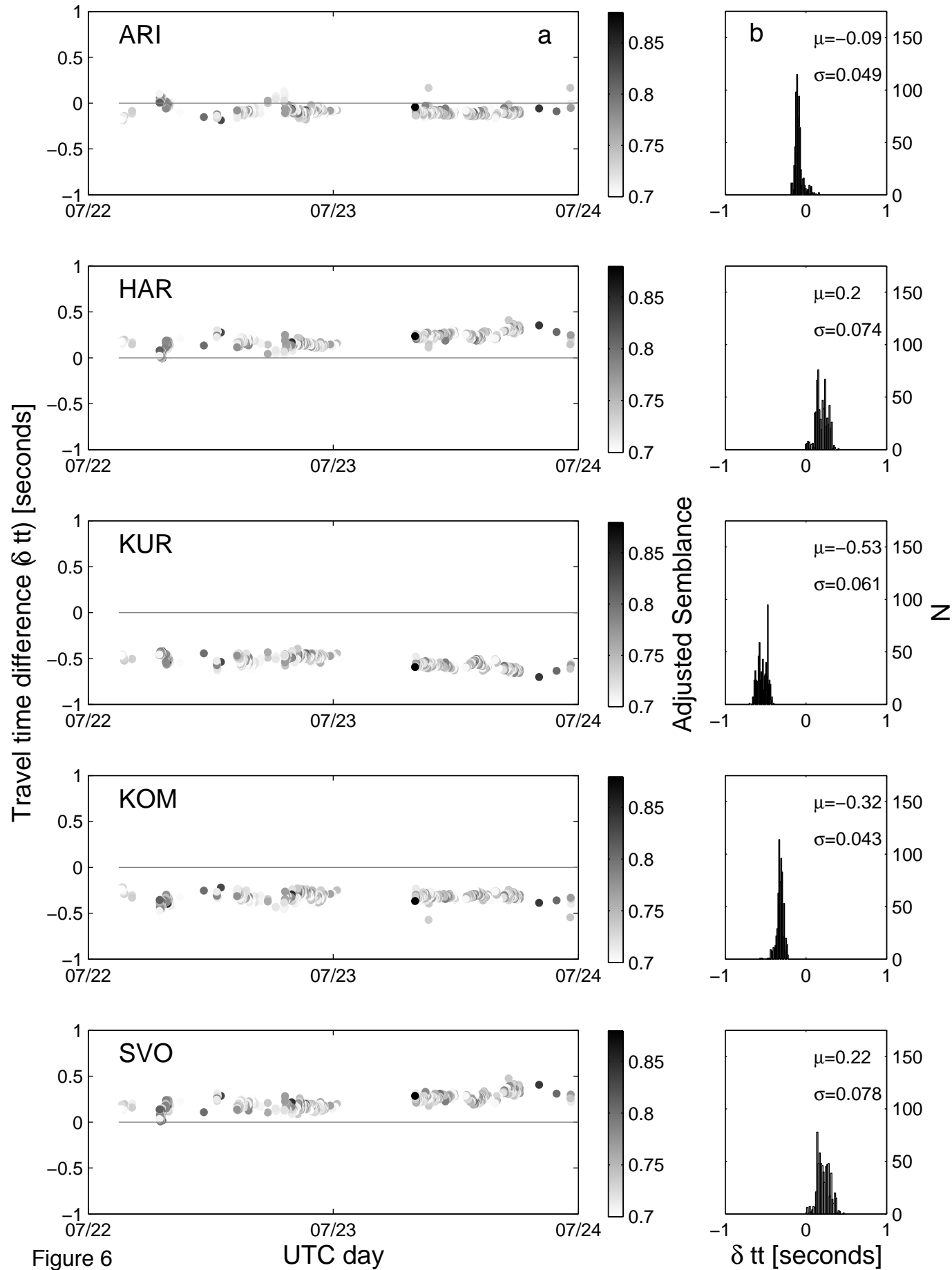


Figure 4







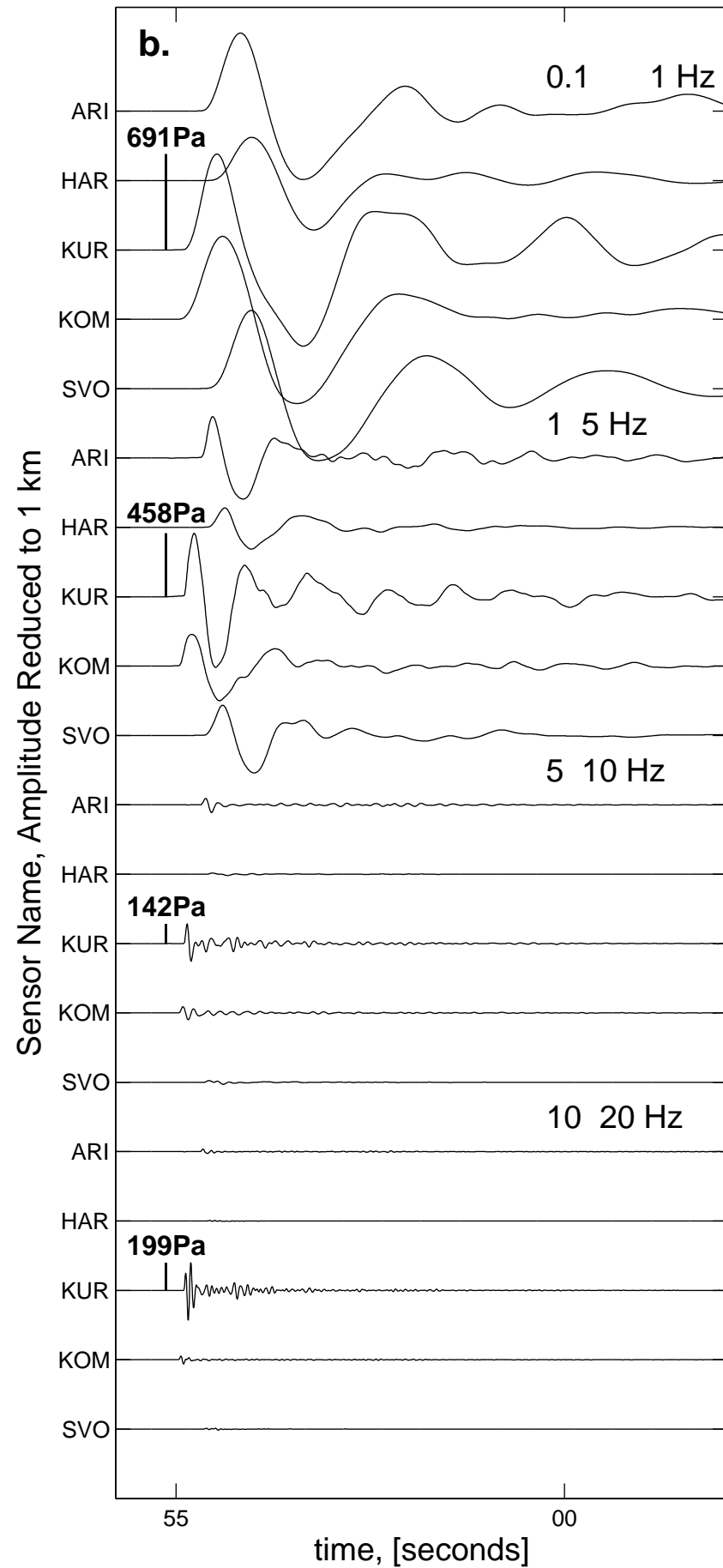
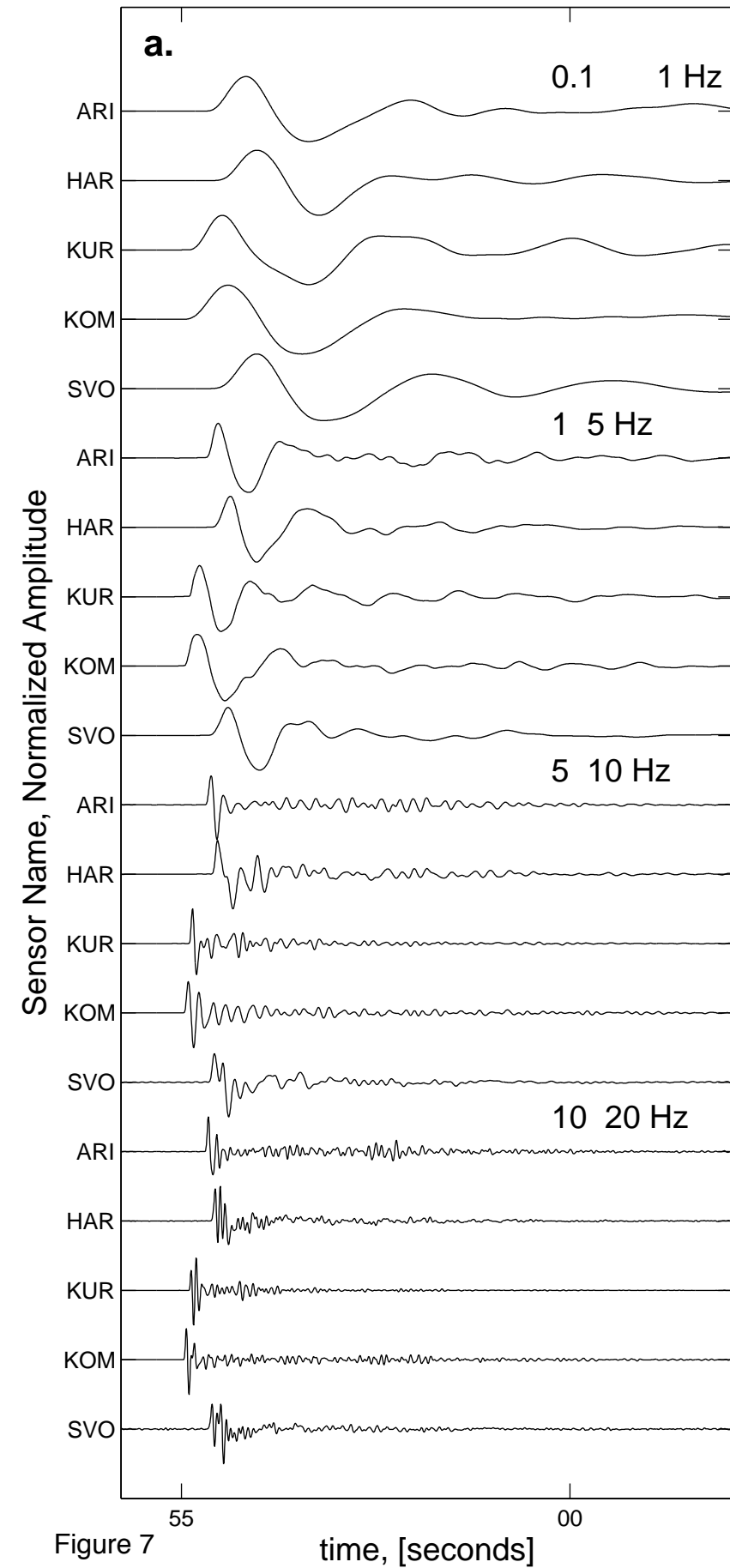


Figure 7

